

3DGAA: Realistic and Robust 3D Gaussian-based Adversarial Attack for Autonomous Driving

Yixun Zhang, Lizhi Wang, Junjun Zhao, Wending Zhao, Feng Zhou, Yonghao Dang, and Jianqin Yin*
 School of Intelligent Engineering and Automation, Beijing University of Posts and Telecommunications, China
 {zhangyixun, wanglizhi, zhaojunjun, windy, zhoulfeng, dyh2018, jqyin}@bupt.edu.cn

Abstract

Camera-based object detection systems play a vital role in autonomous driving, yet they remain vulnerable to adversarial threats in real-world environments. Existing 2D and 3D physical attacks, due to their focus on texture optimization, often struggle to balance physical realism and attack robustness. In this work, we propose **3D Gaussian-based Adversarial Attack (3DGAA)**, a novel adversarial object generation framework that leverages the full 14-dimensional parameterization of 3D Gaussian Splatting (3DGS) to jointly optimize geometry and appearance in physically realizable ways. Unlike prior works that rely on patches or texture optimization, 3DGAA jointly perturbs both geometric attributes (shape, scale, rotation) and appearance attributes (color, opacity) to produce physically realistic and transferable adversarial objects. We further introduce a **physical filtering module** that filters outliers to preserve geometric fidelity, and a **physical augmentation module** that simulates complex physical scenarios to enhance attack generalization under real-world conditions. We evaluate 3DGAA on both virtual benchmarks and physical-world setups using miniature vehicle models. Experimental results show that 3DGAA achieves to reduce the detection mAP from **87.21%** to **7.38%**, significantly outperforming existing 3D physical attacks. Moreover, our method maintains high transferability across different physical conditions, demonstrating a new state-of-the-art in physically realizable adversarial attacks.

1. Introduction

Camera-based object detection systems serve as a cornerstone of autonomous driving [1, 2, 37], enabling essential tasks such as obstacle avoidance and lane navigation. However, increasing researches show that these models are highly vulnerable to adversarial examples. In physical world, subtle, structured perturbations often induce mis-

classifications [4, 10, 11, 28, 30, 46]. This raises serious concerns about the reliability of perception modules in safety-critical scenarios. Thus, systematically exploring such vulnerabilities is essential to understand and improve the real world safety of autonomous driving systems [3, 7, 15, 16, 26, 32, 33, 38–40, 42, 45].

Existing physical adversarial attacks typically fall into two categories: 2D patch-based methods and 3D texture-level attacks. 2D methods typically apply adversarial patches onto objects [3, 7, 15, 38], achieving high physical realism through minimal appearance changes, but often suffer from poor robustness across viewpoints or physical conditions (**Challenge 1**). In contrast, recent 3D attacks [26, 32, 33, 39, 40, 42, 45] achieve stronger and more consistent multi-view adversarial performance by directly manipulating surface textures. However, they often rely solely on appearance perturbations, which may result in visual artifacts or unrealistic surface distortions. This limits their applicability in safety-critical settings, where high physical realism is essential for real-world deployment (**Challenge 2**). This reveals an inherent trade-off between *physical realism* and *adversarial robustness*, posing a key challenge for deploying such attacks in real-world scenarios where both are critical (**Challenge 3**).

To address these challenges, we introduce **3DGAA**, an adversarial attack framework that performs joint optimization of geometric and appearance perturbations to generate physically realistic adversarial objects. This is achieved by leveraging 3D Gaussian Splatting (3DGS) [19], a differentiable and compact 3D representation originally designed for photorealistic rendering. Unlike mesh-based or point-based representations, 3DGS encodes both shape and texture in a unified 14-dimensional parameter space, enabling fine-grained and physically consistent adversarial manipulation [14, 34, 35].

3DGAA comprises three key modules that jointly address the trade-off between physical realism and attack robustness: First, a *Physically-Constrained Adversarial Optimization* stage jointly perturbs geometry and appearance attributes to degrade detector confidence across diverse view-

*Corresponding author.

points and camera distances. This overcomes the limited perturbation scope of 2D methods and addresses **Challenge 1**. Second, we propose a *Physical Filtering Module* that enhances geometric fidelity by removing topological outliers and denoising structural artifacts. This module enforces surface-level consistency and mitigates unrealistic deformations commonly seen in texture-only adversarial models, thereby preserving the visual plausibility of the 3D object from multiple perspectives. It further enhances physical reality, tackling **Challenge 2**. Furthermore, our framework leverages the expressive and differentiable nature of 3DGS to strike a unique balance between these two conflicting objectives. We introduce a *Physical Augmentation Module* that injects environmental variations—such as imaging noise, photometric distortions, shadows, and occlusions—into the optimization loop. This improves generalization under real-world conditions, addressing **Challenge 3**.

Extensive experiments on both virtual benchmarks and real-world miniature vehicle setups validate our approach. Specifically, 3DGAA reduces detection mAP from **87.21%** to **7.38%**, and consistently succeeds across different lighting and viewpoint scenarios. These results demonstrate its strong physical realism and attack robustness. As shown in Fig. 1, 3DGAA achieves superior physical deployment effectiveness and occupies the optimal region in the realism-robustness space, outperforming existing 2D and 3D baselines. Our contributions are summarized as follows:

- We propose **3DGAA**, the novel adversarial framework to adapt 3D Gaussian Splatting for physical adversarial object generation, enabling joint optimization of geometry and appearance in its native parameter space.
- We design two novel modules: a **physical filtering module** leveraging topological pruning and structural denoising to enforce geometric fidelity, and a **physical augmentation module** to simulate environmental conditions and improve robustness in camera-based object detection systems.
- We conduct extensive experiments of the proposed framework, including real-world deployment using miniature vehicle models. The results show a strong attack performance, with a detection degradation of 79.83%, verifying the physical effectiveness and cross-domain transferability of 3DGAA.

2. Related Work

Physical adversarial attacks. In autonomous driving scenarios, physical adversarial attacks aim to deceive real-world perception systems by perturbing object appearance in a deployable manner. Early methods [3, 7, 20, 24, 38] mainly adopt 2D patch-based perturbations rendered on printable surfaces. UPC [15] introduces universal physical patches that generalize across scenarios, DAS [40] exploits differentiable mesh rendering [18] to inject perturba-

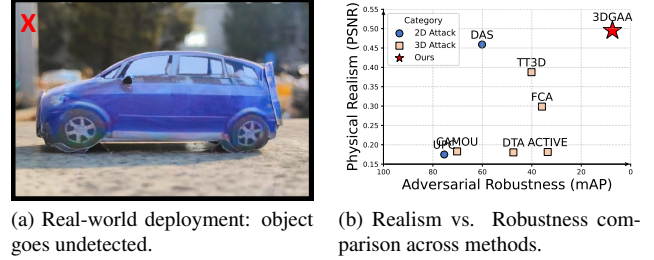


Figure 1. (a) Physical deployment of 3DGAA on a miniature vehicle, resulting in detection failure. (b) Comparison of adversarial methods in terms of physical realism (PSNR) and attack effectiveness (mAP). 3DGAA achieves state-of-the-art performance on both axes.

tion via attention manipulation. Although these approaches offer strong attack performance, they often exhibit limited robustness under varying viewpoints and lighting.

To improve generalization, recent works leverage 3D object representations and render adversarial textures onto full object meshes [32, 39, 40, 42, 45]. In particular, FCA [39] generates full-surface camouflage with physical constraints. Environment-aware enhancements [32, 33] further boost robustness, and recent works such as TT3D [16] and PGA [26] explore high-dimensional texture search spaces.

Despite their improved transferability, most existing physical attacks rely solely on texture perturbations, which limit their expressiveness and fail under geometric distortions or sensor variations [17, 22, 27]. These methods lack the ability to jointly manipulate geometric cues such as shape, scale, or position, factors critical for consistent real-world perception. To overcome this limitation, we propose a new class of physical adversarial attacks that extend beyond appearance-only changes.

Our approach leverages 3D Gaussian Splatting [19], a differentiable and expressive 3D representation, to jointly optimize both geometry and appearance in a unified 14-dimensional space [5, 9, 14, 21, 34]. This formulation enables physically realistic perturbations that remain effective under variable real-world conditions [36, 43]. Unlike prior works constrained to textures, our method introduces perturbation through joint optimization of geometry and appearance, enabling physically realistic and adversarially robust object perturbations for evaluating robust perception systems.

3. Method

3.1. Preliminaries

Formally, we assume access to n multi-view RGB images $\{I_i\}_{i=1}^n$ of a target object, captured under calibrated camera poses $\{P_i\}_{i=1}^n$. These inputs are fed into a pretrained 3D

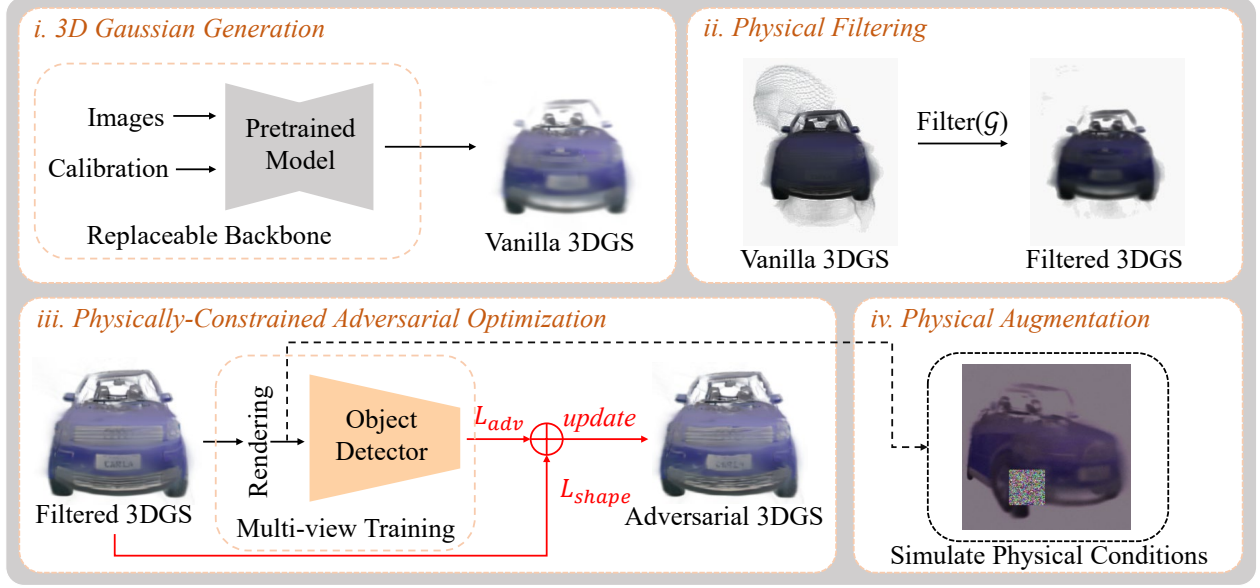


Figure 2. **Overview of the proposed 3DGAA pipeline.** (i) Given multi-view images and camera calibration, a pretrained backbone generates a vanilla 3D Gaussian Splatting (3DGS) object. (ii) A physical filtering module applies topological pruning and structural denoising to improve physical plausibility. (iii) The adversarial optimization stage perturbs the filtered 3DGS using an adversarial loss L_{adv} to deceive object detectors and a shape loss L_{shape} to maintain physical consistency. (iv) The final adversarial 3DGS is trained under physical augmentations including different physical variations.

Gaussian Splatting (3DGS) generation network to generate a base object $\mathcal{G} = \{\mathbf{g}_j\}_{j=1}^N$, where each Gaussian primitive $\mathbf{g}_j \in \mathbb{R}^{14}$ is parameterized by: Position $\mathbf{x} \in \mathbb{R}^3$, Rotation $\mathbf{q} \in \mathbb{R}^4$ (quaternion), Scale $\mathbf{s} \in \mathbb{R}^3$, Color $\mathbf{c} \in \mathbb{R}^3$, Opacity $\alpha \in \mathbb{R}$. This 14-dimensional representation allows for fine-grained control over both geometry and appearance, making it highly suitable for physical adversarial object generation. The 3DGS generation process can be formulated as:

$$\mathcal{G} = \mathcal{F}_{3DGS}(\{I_i, P_i\}_{i=1}^n), \quad (1)$$

where \mathcal{F}_{3DGS} denotes the pretrained Gaussian generation network that maps calibrated RGB images to a set of N Gaussians $\mathcal{G} = \{\mathbf{g}_j\}_{j=1}^N$, with each $\mathbf{g}_j \in \mathbb{R}^{14}$ encoding geometry and appearance attributes.

Optimizing target. Our goal is to perturb the Gaussian parameters such that the object, when rendered into a scene and processed by a detector D , minimizes the predicted confidence for its true class. Let $R(\mathcal{G}, P)$ denote the rendered image from pose P , the core adversarial goal can be formulated as:

$$\min_{\mathcal{G}} L_{adv} = \mathbb{E}_{P \sim \mathcal{V}} [f_D(R(\mathcal{G}, P))] \quad (2)$$

where $f_D(\cdot)$ denotes the detection confidence of the target class and \mathcal{V} denotes a distribution over camera viewpoints.

3.2. Overview

As shown in Figure 2, our proposed **3DGAA** framework generates adversarial 3D objects through a four-stage pipeline: **i. 3D Gaussian Generation:** Multi-view images and camera parameters are fed into a pretrained backbone to generate an initial 3DGS object. **ii. Physical Filtering:** Structural artifacts and topological noise are removed to enhance physical realism. **iii. Adversarial Optimization:** The filtered object is optimized using an adversarial loss L_{adv} and a shape consistency loss L_{shape} . **iv. Physical Augmentation:** Differentiable augmentations simulate environmental conditions to improve real-world robustness. Together, these modules produce adversarial objects that are both physically realistic and robust across diverse viewpoints and environments.

3.3. Physically-Constrained Adversarial Optimization

To address the limited perturbation capability of traditional methods, we propose a physically-constrained adversarial optimization framework that perturbs both the geometry and texture of the 3DGS representation. This high-degree-of-freedom space enables more expressive and robust adversarial behavior under varying physical conditions.

Adversarial Loss. To suppress the detector’s confidence on the target class, we minimize the expected detection score

across multiple viewpoints:

$$\mathcal{L}_{\text{adv}} = \mathbb{E}_{P \sim \mathcal{V}} [f_D(R(\mathcal{G}, P))], \quad (3)$$

where $R(\mathcal{G}, P)$ is the rendered image of \mathcal{G} from camera pose P , and $f_D(\cdot)$ denotes the predicted confidence score of the target object output by the pretrained detector D .

Shape Consistency Loss. To preserve the physical reality of the object’s geometry, we introduce a shape constraint that penalizes deviations from the original structure:

$$\mathcal{L}_{\text{shape}} = \frac{1}{N} \sum_{j=1}^N \|\mathbf{p}_j - \mathbf{p}_{j,0}\|_2^2 + \|\mathbf{s}_j - \mathbf{s}_{j,0}\|_2^2 + \|\mathbf{q}_j \otimes \mathbf{q}_{j,0}^{-1}\|_2^2, \quad (4)$$

where $\mathbf{p}_{j,0}$, $\mathbf{s}_{j,0}$ and $\mathbf{q}_{j,0}$ are the initial position, scale and rotation before optimization. \otimes denotes quaternion multiplication. By using such a shape consistency loss, we can constrain the deformation of 3DGS during the adversarial attack process, making the adversarial perturbation not mainly concentrated in the geometry dimensions, which has a negative impact on physical reality.

Total Loss and Optimization. The final objective combines the adversarial and shape consistency terms:

$$\mathcal{L} = \lambda_{\text{adv}} \cdot \mathcal{L}_{\text{adv}} + \lambda_{\text{shape}} \cdot \mathcal{L}_{\text{shape}}. \quad (5)$$

To dynamically balance attack strength and geometric fidelity, we set λ_{adv} to be inversely proportional to the adversarial loss and λ_{shape} to follow the unnormalized shape deviation. This allows the optimization to prioritize realism when the attack is already strong, and vice versa.

Algorithm 1 summarizes the optimization loop. The 3DGS parameters are iteratively updated via gradient descent, where each iteration involves rendering, applying physical augmentations, computing adversarial and shape losses, and selectively applying gradients to relevant parameter subsets. The dynamic weights λ_{adv} and λ_{shape} are adjusted according to the magnitude of the current loss to balance the strength of the attack and the preservation of the realism. Further details are provided in Appendix A.1.

3.4. Physical Filtering Module

Despite the flexibility of 3DGS representations, direct optimization over the entire parameter space often results in artifacts such as isolated floating Gaussians and spatial jitter. These issues compromise the physical reality of the resulting objects, especially under multi-view rendering. We propose a Physical Filtering Module to refine the optimized 3D object and enforce geometric consistency.

Topological Pruning (TP). We first remove outlier Gaussians based on projected spatial density. For each Gaussian, we compute its neighborhood density in screen space across sampled viewpoints. If a Gaussian is consistently located in

sparse regions or lacks sufficient overlap with other primitives, it is discarded. This step eliminates fragmented components and prevents unnatural floaters from appearing in rendered views.

Structural Denoising (SD). We further smooth the object by adjusting the scale of neighboring Gaussians to reduce abrupt local variations. We apply a Gaussian-weighted smoothing filter over scale dimension, guided by projected image-space distance and opacity. This encourages gradual transitions in apparent size and reduces aliasing artifacts caused by irregular primitive distribution.

Formally, the filtering process involves (1) pruning low-density Gaussians based on adaptive neighborhood analysis, and (2) applying a structural smoothing function in scales and opacities. Full algorithmic details are provided in Appendix A.2.

3.5. Physical Augmentation Module

To improve the real-world transferability of adversarial 3D objects, we introduce a differentiable *Physical Augmentation Module* that simulates deployment-time environmental variations. This module injects physically realistic perturbations into rendered views during optimization and is composed of four sub-transforms:

Imaging Degradation. We simulate sensor noise and lens blur through depth-aware Gaussian noise $\mathcal{T}_{\text{noise}}$, where the noise level increases with object-camera distance. This models degradation from low-quality hardware or atmospheric scattering.

Photometric Variation. We apply color distortions via channel-wise affine transforms $\mathcal{T}_{\text{photo}}$, introducing random brightness and contrast changes to emulate lighting inconsistencies, exposure drift, and white balance variation.

Shadow Projection. To account for natural illumination effects, we simulate soft shadow overlays using depth-based sigmoid masks $\mathcal{T}_{\text{shadow}}$. These synthetic shadows mimic occlusion by other objects or self-casting.

Adaptive Occlusion. We introduce random rectangular occluders with variable transparency $\mathcal{T}_{\text{occl}}$ to simulate real-world clutter and partial obstructions, enhancing robustness to unexpected foreground elements.

Each transformation is applied in sequence to the rendered image: $\mathcal{T} = \mathcal{T}_{\text{occl}} \circ \mathcal{T}_{\text{shadow}} \circ \mathcal{T}_{\text{photo}} \circ \mathcal{T}_{\text{noise}}$. All operations are differentiable and applied online at every training epoch, allowing gradients to flow through the augmentation pipeline. This enables adversarial optimization to produce samples that remain effective under realistic sensing and environmental distortions. Additional formulation details are provided in Appendix A.3.

3.6. Selective Dimension Optimization

To support flexible adversarial sample generation under physical constraints, we introduce a manual dimension se-

Algorithm 1 Adversarial 3DGS Optimization

Require: T : Total iterations
 θ_0 : Initial 3DGS parameters
 $R(\cdot)$: 3DGS differentiable renderer
 $\mathcal{T}(\cdot)$: Physical augmentation function
 \mathcal{L}_{adv} : Adversarial loss
 $\mathcal{L}_{\text{shape}}$: Shape consistency loss
 \mathcal{K} : Selected dimensions for update

Ensure: Optimized 3DGS parameters θ

- 1: $\theta \leftarrow \theta_0$ ▷ Initialization
- 2: **for** $t = 1$ **to** T **do**
- 3: $I \leftarrow R(\theta)$ ▷ Render current 3DGS
- 4: $\tilde{I} \leftarrow \mathcal{T}(I)$ ▷ Apply physical augmentation
- 5: Compute weights $\lambda_{\text{adv}}, \lambda_{\text{shape}}$ based on current loss values
- 6: $\delta \leftarrow \nabla_{\theta} [\lambda_{\text{adv}} \cdot \mathcal{L}_{\text{adv}}(\tilde{I}) + \lambda_{\text{shape}} \cdot \mathcal{L}_{\text{shape}}(\theta)]$
- 7: $\theta \leftarrow \theta - \text{Mask}_{\mathcal{K}}(\delta)$ ▷ Update selected dimensions only
- 8: **end for**
- 9: **return** θ

lection strategy that decouples geometric and appearance parameters in the 3DGS space. Specifically, users can define a subset of dimensions $K \subset \{1, \dots, 14\}$ to be optimized, allowing certain parameters to remain fixed based on deployment requirements. This design enables tailored perturbation control across different real-world scenarios. For instance, one may constrain geometry when targeting printable objects or preserve opacity to ensure sensor transparency. The strategy also provides practical benefits in training efficiency and transferability, as further validated in Section 4.5. Implementation details and additional visualizations are deferred to Appendix A.4 for clarity.

4. Experiments

4.1. Experimental Setup

Baseline Methods. We compare 3DGAA against representative open-source 2D and 3D physical attack baselines, including CAMOU[45], UPC[15], DAS[40], FCA[39], DTA[32], ACTIVE[33] and TT3D[16]. For a fair comparison, all methods are adapted to the same synthetic and real-world setups with standard calibration and consistent rendering settings.

Generation Pipeline and Camera Setup. For digital rendering, we use a differentiable 3D Gaussian renderer following [34]. All adversarial objects are rendered under multi-view camera settings, with 12 evenly spaced azimuth angles and 3 distances (3m, 5m, 10m), simulating realistic surveillance conditions. For physical-world evaluation, we deploy textured miniature models under varied lighting conditions and capture images using a Realme GT Neo5 SE

camera mounted on a motorized rig with fixed focal length in a proportionally reduced distance.

Target Models. We evaluate detection attacks on six widely used object detectors: Faster R-CNN [31], Mask R-CNN [13], SSD [23], YOLOv3 [29], YOLOv5 and YOLOv8. For transferable task segmentation, we use DeepLabv3 [6] and FCN [25] with ResNet-50 and ResNet-101 [12] backbones.

Evaluation Metrics. We report attack effectiveness using the **Log Confidence Reduction (LCR)**, which measures the proportion of images where the detector fails to assign the correct label to the adversarial object. LCR is defined as:

$$\text{LCR} = \log \left(\frac{\text{Initial Confidence}}{\text{Final Confidence}} \right). \quad (6)$$

Unlike absolute confidence drop, LCR normalizes adversarial effectiveness across different baselines, ensuring a fairer comparison. We also report mean Average Precision with 50% threshold (**mAP@0.5**) to reflect detection performance decline. To quantify physical realism, we adopt image similarity metrics including **LPIPS** [44], **SSIM** [41], and **PSNR**, computed between rendered adversarial objects and their original clean versions.

Implementation Details. All experiments are conducted on a single NVIDIA RTX 4090 GPU. We set the number of epochs in 50, the attack training finished in 1 minute (see Appendix C.3). The two loss terms in our objective—adversarial loss \mathcal{L}_{adv} and shape consistency loss $\mathcal{L}_{\text{shape}}$ —are dynamically weighted during optimization. Specifically, we compute the relative loss magnitudes and normalize them to balance gradients: the weight for \mathcal{L}_{adv} is inversely proportional to its scaled loss value, while the weight for $\mathcal{L}_{\text{shape}}$ is proportional to its raw value. This dynamic scheme eliminates the need for manual tuning of fixed loss weights.

4.2. Comprehensive Comparison with Benchmark Physical Attacks

We compare 3DGAA with a range of representative physical adversarial attack methods, including both 2D patch-based and 3D texture-based approaches. Our evaluation considers two key dimensions: *physical realism*, how visually consistent the adversarial object is with its original counterpart, and *attack effectiveness*, how successfully it deceives object detection models.

Physical Realism. As shown in Table 1, 3DGAA achieves the lowest LPIPS score (0.5373), indicating minimal perceptual distortion and high-fidelity texture appearance. While our SSIM score is marginally lower than that of UPC, this is primarily due to the inherent approximation in 3DGS-based geometry rather than the adversarial manipulation. In particular, 3DGAA achieves the highest PSNR

Table 1. **Benchmark Comparison** of 3DGAA and existing baseline adversarial attack methods. Our method 3DGAA achieves the best performance across almost all metrics, demonstrating superior physical realism and adversarial robustness.

Method	Vanilla	CAMOU[45]	UPC[15]	DAS[40]	FCA[39]	DTA[32]	ACT.[33]	TT3D[16]	3DGAA
LPIPS ↓	0.0000	0.6210	0.6161	0.5979	0.5629	0.6142	0.6105	0.5433	0.5373
SSIM ↑	1.0000	0.0212	0.0224	0.0132	0.0123	0.0198	0.0193	0.0122	0.0128
PSNR ↑	∞	0.1829	0.1749	0.4590	0.2987	0.1804	0.1814	0.3876	0.4951
LCR ↑	0.0000	0.3128	0.2095	0.5366	1.2810	0.8784	1.3778	1.1202	3.5628
mAP ↓	87.21%	70.21%	75.42%	60.12%	35.89%	47.44%	33.56%	40.12%	7.38%

value among attack methods, reflecting superior preservation of pixel-level fidelity during optimization. These results demonstrate the benefit of our shape loss and physical filtering module in maintaining object realism.

Attack Strength. 3DGAA significantly outperforms all baselines in terms of adversarial robustness in Table 1. It achieves an LCR of 3.5628, far exceeding the second-best method (ACTIVE at 1.3778), and reduces the detector’s mAP from 87.21% to just 7.38%. This indicates that our method not only fools the detector more often, but also leads to lower residual confidence, effectively suppressing recognition. These results validate the effectiveness of simultaneously optimizing both geometric and appearance parameters in the 3DGS space, enabling stronger and more transferable adversarial effects.

Viewpoint Robustness. We evaluate attack consistency by rendering adversarial objects from multiple viewpoints. As shown in Figure 3, the original object is consistently detected (top), while the 3DGAA version evades or misleads detection from all views (bottom). We also measure LCR across 12 azimuth angles and 3 distances. Figure 4 shows higher success rates at side views and close range, with performance slightly declining under front views or long distances, validating the multi-view training strategy and 3DGAA’s robustness to viewpoint variations.

Together, these results confirm that 3DGAA achieves strong attack success while preserving physical realism, and remains effective under diverse viewpoints, which are key properties for physically deployable adversarial objects.

4.3. Effectiveness of the Physical Filtering Module

To evaluate the impact of the physical filtering module introduced in Section 3.4, we compare the results of applying topology pruning (TP), structural denoising (SD), and their combination. As shown in Figure 5, the visual artifacts, such as floating Gaussians and irregular surface patches, are significantly reduced after filtering. The TP step removes geometric outliers, while SD smooths local scale inconsistencies. The combined TP+SD strategy yields the cleanest geometry and most plausible object structure.

Quantitatively, Table 2 shows that TP+SD improves perceptual realism (LPIPS: 0.5373), achieves the highest SSIM

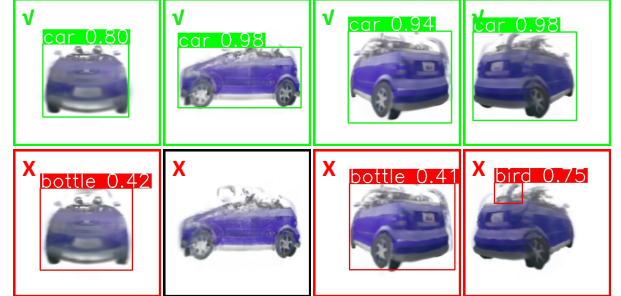


Figure 3. **Multi-Angle Adversarial Attack Effectiveness:** Top row shows original samples with successful detection (green boxes) across different viewpoints. Bottom row demonstrates 3DGAA-generated adversarial textures evading detection (black boxes) or false detection (red boxes) at corresponding angles. The consistent performance across viewing perspectives highlights 3DGAA robustness to viewpoint variations.

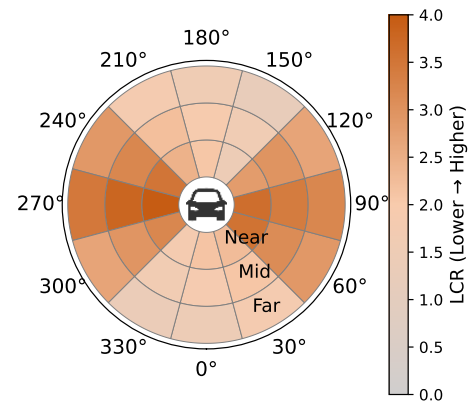


Figure 4. Polar plot of LCR across 12 viewpoints and 3 distances in simulation. Attacks are most effective at side views and short range.

(0.0128) and removes 83.1% of artifacts, although with a slight decrease in PSNR due to suppression of high-frequency noise. This trade-off is acceptable, as it prioritizes geometric plausibility over strict pixel-level fidelity, aligning with our goal of producing physically realistic adversarial objects.

Table 2. Filtering strategy comparison across different metrics. TP+SD achieves the best performance on physical realism and artifacts removal (AR).

Method	LPIPS ↓	SSIM ↑	PSNR ↑	AR (%) ↑
Vanilla	0.5443	0.0105	0.5282	0.0
TP	0.5435	0.0086	0.5251	19.8
SD	0.5386	0.0121	0.5015	72.2
TP + SD	0.5373	0.0128	0.4951	83.1

Table 3. Ablation study of the shape loss component. \mathcal{L}_{adv} + \mathcal{L}_{shape} achieves the best physical realism.

Method	LPIPS ↓	SSIM ↑	PSNR ↑
\mathcal{L}_{adv} only	0.5516	0.0141	0.5884
\mathcal{L}_{adv} + \mathcal{L}_{shape}	0.5503	0.0146	0.5881

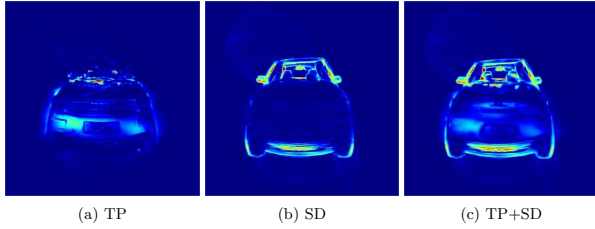


Figure 5. **Geometric refinement analysis through physical filtering module:** (a) Topology pruning (b) Structural denoising (c) Topology pruning + Structural denoising. Color scale indicates local deformation energy. Note the artifacts above and below of the car, which are most obvious in (c), indicating the best removal effect.

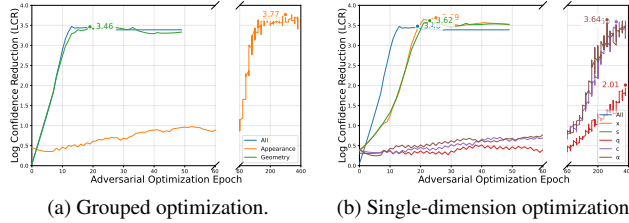


Figure 6. LCR sensitivity analysis. (a) Optimizing geometry dimensions leads to faster convergence, while texture yields higher final LCR. (b) Position and scale are most sensitive; rotation has minimal effect.¹

4.4. Effect of Shape Loss Design

We conduct an ablation study to assess the contribution of the shape loss \mathcal{L}_{shape} introduced in Section 3.3. This loss aims to preserve geometric consistency while optimizing for adversarial effectiveness.

¹The broken axis does not indicate discontinuous data, but compresses the horizontal scale to better visualize post-60-epoch results.



Figure 7. **Physical-world adversarial attack under varying lighting.** Column: ID, IN, OD, ON. Row 1: vanilla, Row 2: w/o Aug., Row 3: w/ Aug. Only the fully augmented adversarial object consistently evades detection.

As shown in Table 3, adding the shape loss slightly improves LPIPS (0.5516 to 0.5503) and SSIM (0.0141 to 0.0146), indicating better perceptual quality and structural preservation. The PSNR value remains similar, with only a minor drop, reflecting a shift from pixel-level perturbation to more physically realistic adjustments. These results show that incorporating \mathcal{L}_{shape} helps balance attack robustness and physical realism, aligning with our dual-objective design.

4.5. Selective Dimension Optimization

To analyze the sensitivity and effectiveness of individual 3DGS parameters during adversarial optimization, we perform a set of experiments that isolate geometric and appearance dimensions.

As shown in Figure 6a, optimizing geometric parameters (position x , scale s) leads to rapid increases in Log Confidence Reduction (LCR), achieving strong attack effectiveness within 30 epochs. In contrast, optimizing texture parameters (opacity α , color c) requires more iterations but ultimately reaches comparable or higher LCR. This suggests a time-performance trade-off: geometry enables fast convergence, while texture offers stronger long-term perturbation due to its direct effect on visual semantics.

A detailed dimension-wise analysis in Figure 6b further reveals that position x and scale s are the most sensitive parameters, contributing significantly to early-stage attack progress. Opacity α and color c exhibit moderate sensitivity, as they influence visibility and texture realism, respectively. Rotation q , despite affecting global geometry, shows minimal impact, due to its non-local and redundant nature in Gaussian-based representations. These findings validate our design of selective dimension optimization (Section 3.6), which allow practitioners to balance com-

Table 4. LCR (\uparrow) for adversarial objects optimized on one detector and tested across others. 3DGAA achieves strong cross-detector generalization.

Method	F-RCNN	M-RCNN	SSD
F-RCNN	2.819	2.111	2.193
M-RCNN	2.841	2.417	2.232
SSD	1.054	0.765	2.349
Method	YOLOv3	YOLOv5	YOLOv8
F-RCNN	6.098	4.684	4.429
M-RCNN	6.180	4.852	4.418
SSD	5.199	3.619	3.210

Table 5. LCR (\uparrow) of segmentation models under 3DGAA attack. 3DGAA achieves strong performance on segmentation models.

Method	DLv3-R50	DLv3-R101	FCN-R50	FCN-R101
LCR	0.628	0.874	0.795	0.893

DLv3: DeepLabV3; R50/101: ResNet-50/101 backbones.

putational efficiency and physical feasibility in real-world deployments. Additional explanations and visual examples are provided in Appendix B.3.

4.6. Transferability Across Models and Tasks

We evaluate the transferability of 3DGAA adversarial objects across different perception models, including detectors with diverse architectures and segmentation models.

Cross-Detector Generalization. Table 4 reports the LCR performance of adversarial objects optimized on one detector and tested on others. Perturbations generated from two-stage detectors (Faster R-CNN and Mask R-CNN) demonstrate strong transferability, reaching LCR = 6.180 on YOLOv3 and maintaining performance on SSD (e.g., F-RCNN \rightarrow SSD yields LCR = 2.193). These results suggest that 3DGAA captures transferable vulnerabilities across architectures through multi-dimensional optimization, rather than overfitting to a specific detector.

Segmentation Attack. We further test 3DGAA’s generalization to segmentation models by evaluating LCR on DeepLabV3 and FCN with ResNet backbones. As shown in Table 5, the attacks transfer reasonably well to segmentation settings, despite being optimized for detection. Interestingly, deeper backbones (ResNet-101) appear more vulnerable than ResNet-50 variants, suggesting that network depth may increase susceptibility to 3D physical perturbations.

4.7. Physical Realization

To verify the real-world effectiveness of 3DGAA, we conduct physical deployment experiments using miniature 3D-

Table 6. Physical-world AP@0.5 (\downarrow) comparison of attack methods. 3DGAA achieves superior physical adversarial effectiveness.

Method	YOLOv5	SSD	F-RCNN	M-RCNN
Vanilla	93.75	84.17	96.25	94.58
Random	80.00	76.25	87.50	82.50
CAMOU [45]	69.58	64.58	72.08	74.17
DAS [40]	75.83	74.17	79.58	77.50
FCA [39]	60.83	48.33	62.92	67.92
3DGAA	32.08	17.92	35.83	34.58

printed vehicles under four lighting conditions: indoor daylight (ID), indoor night (IN), outdoor daylight (OD), and outdoor night (ON). As illustrated in Figure 7, we compare three texture variants: (1) vanilla (non-adversarial), (2) 3DGAA without physical augmentation, and (3) 3DGAA with augmentation. The vanilla object is reliably detected across all conditions. In contrast, 3DGAA w/o Aug. only slightly reduces detection confidence, particularly under lighting. The full 3DGAA w/ Aug. achieves consistent detection failures or misclassifications across all four scenarios. These results demonstrate the critical role of the physical augmentation module in bridging the sim-to-real gap.

We further report AP@0.5 across four detectors in Table 6. 3DGAA significantly reduces AP under real-world imaging from 84.17% to as low as 17.92%, surpassing all baseline physical attacks. This validates the full pipeline’s ability to generate physically robust adversarial objects deployable in uncontrolled physical environments.

5. Conclusion

We present **3DGAA**, a novel adversarial object generation framework that jointly optimizes geometry and appearance in the 3D Gaussian space. Unlike prior methods, 3DGAA enables expressive, multi-view-consistent adversarial robustness. Furthermore, we propose a *Physical Filtering Module* for physical realism and a *Physical Augmentation Module* for simulating environmental to develop real-world deployment. Extensive experiments show that 3DGAA significantly degrades detection performance (mAP \downarrow to 7.38%) while maintaining strong physical realism across detectors and environments. It also generalizes across viewpoints, model architectures, and segmentation tasks, validating 3DGAA as a robust and transferable pipeline for evaluating safety-critical perception systems, especially in autonomous driving scenarios.

A detailed discussion of security concerns and potential societal risks and mitigation strategies is included in Appendix C.4.

References

- [1] Baidu Apollo, 2020. <http://apollo.auto/>. 1
- [2] Autoware.ai, 2020. <https://www.autoware.ai/>. 1
- [3] Tom B. Brown, Dandelion Mané, Aurko Roy, Martín Abadi, and Justin Gilmer. Adversarial patch, 2018. 1, 2
- [4] Nicholas Carlini and David Wagner. Towards evaluating the robustness of neural networks. In *2017 IEEE Symposium on Security and Privacy (SP)*, 2017. 1
- [5] Guikun Chen and Wenguan Wang. A survey on 3d gaussian splatting, 2025. 2
- [6] Liang-Chieh Chen, George Papandreou, Florian Schroff, and Hartwig Adam. Rethinking atrous convolution for semantic image segmentation, 2017. 5
- [7] Shang-Tse Chen, Cory Cornelius, Jason Martin, and Duen Horng (Polo) Chau. Shapeshifter: Robust physical adversarial attack on faster r-cnn object detector. In *Machine Learning and Knowledge Discovery in Databases: European Conference, ECML PKDD 2018, Dublin, Ireland, September 10–14, 2018, Proceedings, Part I*, page 52–68, Berlin, Heidelberg, 2018. Springer-Verlag. 1, 2
- [8] Alexey Dosovitskiy, German Ros, Felipe Codevilla, Antonio Lopez, and Vladlen Koltun. CARLA: An open urban driving simulator. In *Proceedings of the 1st Annual Conference on Robot Learning (CoRL)*, pages 1–16, 2017. 3
- [9] Ben Fei, Jingyi Xu, Rui Zhang, Qingyuan Zhou, Weidong Yang, and Ying He. 3d gaussian splatting as new era: A survey. *IEEE Transactions on Visualization and Computer Graphics*, pages 1–20, 2024. 2
- [10] Andreas Geiger, Philip Lenz, and Raquel Urtasun. Are we ready for autonomous driving? the kitti vision benchmark suite. In *2012 IEEE Conference on Computer Vision and Pattern Recognition (CVPR)*, pages 3354–3361, 2012. 1
- [11] Ian J. Goodfellow, Jonathon Shlens, and Christian Szegedy. Explaining and harnessing adversarial examples, 2015. 1
- [12] Kaiming He, Xiangyu Zhang, Shaoqing Ren, and Jian Sun. Deep residual learning for image recognition, 2015. 5
- [13] Kaiming He, Georgia Gkioxari, Piotr Dollár, and Ross Girshick. Mask r-cnn. In *2017 IEEE International Conference on Computer Vision (ICCV)*, pages 2980–2988, 2017. 5
- [14] Yicong Hong, Kai Zhang, Jiuxiang Gu, Sai Bi, Yang Zhou, Difan Liu, Feng Liu, Kalyan Sunkavalli, Trung Bui, and Hao Tan. Lrm: Large reconstruction model for single image to 3d, 2024. 1, 2
- [15] Lifeng Huang, Chengying Gao, Yuyin Zhou, Cihang Xie, Alan L. Yuille, Changqing Zou, and Ning Liu. Universal physical camouflage attacks on object detectors. In *2020 IEEE/CVF Conference on Computer Vision and Pattern Recognition (CVPR)*, 2020. 1, 2, 5, 6
- [16] Yao Huang, Yinpeng Dong, Shouwei Ruan, Xiao Yang, Hang Su, and Xingxing Wei. Towards transferable targeted 3d adversarial attack in the physical world. In *2020 IEEE/CVF Conference on Computer Vision and Pattern Recognition (CVPR)*, pages 24512–24522, 2024. 1, 2, 5, 6
- [17] Matthew Hull, Chao Zhang, Zsolt Kira, and Duen Horng Chau. Adversarial attacks using differentiable rendering: A survey, 2024. 2
- [18] Hiroharu Kato, Yoshitaka Ushiku, and Tatsuya Harada. Neural 3d mesh renderer. In *2018 IEEE/CVF Conference on Computer Vision and Pattern Recognition (CVPR)*, 2018. 2
- [19] Bernhard Kerbl, Georgios Kopanas, Thomas Leimkühler, and George Drettakis. 3d gaussian splatting for real-time radiance field rendering. *ACM Transactions on Graphics*, 42(4), 2023. 1, 2
- [20] Mark Lee and Zico Kolter. On physical adversarial patches for object detection, 2019. 2
- [21] Longwei Li, Huajian Huang, Sai-Kit Yeung, and Hui Cheng. Omnigs: Fast radiance field reconstruction using omnidirectional gaussian splatting. In *Proceedings of the Winter Conference on Applications of Computer Vision (WACV)*, pages 2260–2268, 2025. 2
- [22] Yanjie Li, Bin Xie, Songtao Guo, Yuanyuan Yang, and Bin Xiao. A survey of robustness and safety of 2d and 3d deep learning models against adversarial attacks. *ACM Comput. Surv.*, 56(6), 2024. 2
- [23] Wei Liu, Dragomir Anguelov, Dumitru Erhan, Christian Szegedy, Scott Reed, Cheng-Yang Fu, and Alexander C. Berg. SSD: Single shot multibox detector. In *2016 European Conference on Computer Vision (ECCV)*, 2016. 5
- [24] Xin Liu, Huanrui Yang, Linghao Song, Hai Li, and Yiran Chen. Dpatch: Attacking object detectors with adversarial patches. *CoRR*, abs/1806.02299, 2, 2018. 2
- [25] Jonathan Long, Evan Shelhamer, and Trevor Darrell. Fully convolutional networks for semantic segmentation. In *2015 IEEE Conference on Computer Vision and Pattern Recognition (CVPR)*, 2015. 5
- [26] Tianrui Lou, Xiaojun Jia, Siyuan Liang, Jiawei Liang, Ming Zhang, Yanjun Xiao, and Xiaochun Cao. 3d gaussian splatting driven multi-view robust physical adversarial camouflage generation, 2025. 1, 2
- [27] Qiming Lu, Shikui Wei, Haoyu Chu, and Yao Zhao. Towards transferable 3d adversarial attack. In *Proceedings of the 3rd ACM International Conference on Multimedia in Asia (MMAsia)*, New York, NY, USA, 2022. Association for Computing Machinery. 2
- [28] Kien Nguyen, Tharindu Fernando, Clinton Fookes, and Sridha Sridharan. Physical adversarial attacks for surveillance: A survey. *IEEE Transactions on Neural Networks and Learning Systems (TNNLS)*, 35(12):17036–17056, 2024. 1
- [29] Joseph Redmon and Ali Farhadi. Yolo3: An incremental improvement, 2018. 5
- [30] Huali Ren and Teng Huang. Adversarial example attacks in the physical world. In *Machine Learning for Cyber Security*, pages 572–582, Cham, 2020. Springer International Publishing. 1
- [31] Shaoqing Ren, Kaiming He, Ross Girshick, and Jian Sun. Faster r-cnn: Towards real-time object detection with region proposal networks. *IEEE Transactions on Pattern Analysis and Machine Intelligence (PAMI)*, 39(6):1137–1149, 2017. 5
- [32] Naufal Suryanto, Yongsu Kim, Hyoeun Kang, Harashta Tatimma Larasati, Youngyeo Yun, Thi-Thu-Huong Le, Hunmin Yang, Se-Yoon Oh, and Howon Kim. Dta: Physical camouflage attacks using differentiable transformation network. In *Proceedings of the IEEE/CVF Conference*

- on *Computer Vision and Pattern Recognition (CVPR)*, pages 15305–15314, 2022. 1, 2, 5, 6
- [33] Naufal Suryanto, Yongsu Kim, Harashta Tatimma Larasati, Hyoeun Kang, Thi-Thu-Huong Le, Yoonyoung Hong, Hunmin Yang, Se-Yoon Oh, and Howon Kim. Active: Towards highly transferable 3d physical camouflage for universal and robust vehicle evasion. In *2023 IEEE/CVF International Conference on Computer Vision (ICCV)*, pages 4282–4291, 2023. 1, 2, 5, 6
- [34] Jiaxiang Tang, Zhaoxi Chen, Xiaokang Chen, Tengfei Wang, Gang Zeng, and Ziwei Liu. Lgm: Large multi-view gaussian model for high-resolution 3d content creation, 2024. 1, 2, 5, 3
- [35] Jiaxiang Tang, Jiawei Ren, Hang Zhou, Ziwei Liu, and Gang Zeng. Dreamgaussian: Generative gaussian splatting for efficient 3d content creation. In *The Twelfth International Conference on Learning Representations (ICLR)*, 2024. 1
- [36] Ziyu Tang, Weicai Ye, Yifan Wang, Di Huang, Hujun Bao, Tong He, and Guofeng Zhang. Nd-sdf: Learning normal deflection fields for high-fidelity indoor reconstruction. In *2025 International Conference on Learning Representations (ICLR)*, pages 3460–3489, 2025. 2
- [37] Tesla, 2025. <https://www.tesla.com/fsd/>. 1
- [38] Simen Thys, Wiebe Van Ranst, and Toon Goedeme. Fooling automated surveillance cameras: adversarial patches to attack person detection. In *2019 IEEE/CVF Conference on Computer Vision and Pattern Recognition Workshops (CVPRW)*, 2019. 1, 2
- [39] Donghua Wang, Tingsong Jiang, Jialiang Sun, Weien Zhou, Zhiqiang Gong, Xiaoya Zhang, Wen Yao, and Xiaoqian Chen. Fca: Learning a 3d full-coverage vehicle camouflage for multi-view physical adversarial attack. *Proceedings of the AAAI Conference on Artificial Intelligence*, page 2414–2422, 2022. 1, 2, 5, 6, 8
- [40] Jiakai Wang, Aishan Liu, Zixin Yin, Shunchang Liu, Shiyu Tang, and Xianglong Liu. Dual attention suppression attack: Generate adversarial camouflage in physical world. In *2021 IEEE/CVF Conference on Computer Vision and Pattern Recognition (CVPR)*, 2021. 1, 2, 5, 6, 8
- [41] Zhou Wang, A.C. Bovik, H.R. Sheikh, and E.P. Simoncelli. Image quality assessment: from error visibility to structural similarity. *IEEE Transactions on Image Processing*, 13(4): 600–612, 2004. 5
- [42] Tong Wu, Xuefei Ning, Wenshuo Li, Ranran Huang, Huazhong Yang, and Yu Wang. Physical adversarial attack on vehicle detector in the carla simulator, 2020. 1, 2
- [43] Jason Y. Zhang, Amy Lin, Moneish Kumar, Tzu-Hsuan Yang, Deva Ramanan, and Shubham Tulsiani. Cameras as rays: Pose estimation via ray diffusion. In *The Twelfth International Conference on Learning Representations (ICLR)*, 2024. 2
- [44] Richard Zhang, Phillip Isola, Alexei A Efros, Eli Shechtman, and Oliver Wang. The unreasonable effectiveness of deep features as a perceptual metric. In *2018 IEEE/CVF Conference on Computer Vision and Pattern Recognition (CVPR)*, 2018. 5
- [45] Yang Zhang, Hassan Foroosh, Philip David, and Boqing Gong. Camou: Learning physical vehicle camouflages to adversarially attack detectors in the wild. *International Conference on Learning Representations (ICLR)*, 2018. 1, 2, 5, 6, 8
- [46] Heran Zhu and Dazhong Rong. Multiview consistent physical adversarial camouflage generation through semantic guidance. In *2024 International Joint Conference on Neural Networks (IJCNN)*, pages 1–8, 2024. 1

3DGAA: Realistic and Robust 3D Gaussian-based Adversarial Attack for Autonomous Driving

Supplementary Material

More details on the method, experimental, and a discussion of some extended questions are included in this supplementary material.

A. Supplementary of Methods

Note that the selected intermediate physical derivations have been condensed for conciseness.

A.1. Dynamic Loss Weighting Strategy

To ensure stable optimization between the adversarial objective \mathcal{L}_{adv} and the shape consistency loss $\mathcal{L}_{\text{shape}}$, we employ a dynamic weighting mechanism that adaptively balances the two terms based on their magnitudes.

Let $\bar{\mathcal{L}}_{\text{adv}}$ and $\bar{\mathcal{L}}_{\text{shape}}$ denote the average adversarial loss and shape loss at a given iteration. We first scale the adversarial loss for numerical stability:

$$\hat{\mathcal{L}}_{\text{adv}} = \bar{\mathcal{L}}_{\text{adv}} / \gamma, \quad (\text{A.1})$$

where γ is a scale factor (set to 10.0 in our experiments).

We then compute unnormalized weights:

$$w_{\text{adv}} = \frac{1}{\hat{\mathcal{L}}_{\text{adv}} + \varepsilon}, \quad w_{\text{shape}} = \bar{\mathcal{L}}_{\text{shape}}, \quad (\text{A.2})$$

where ε is a small constant to avoid division by zero.

The raw weights are normalized:

$$\lambda_{\text{adv}} = \frac{w_{\text{adv}}}{w_{\text{adv}} + w_{\text{shape}} + \varepsilon}, \quad \lambda_{\text{shape}} = 1 - \lambda_{\text{adv}}. \quad (\text{A.3})$$

To prevent collapse into one objective, we clamp λ_{shape} to a minimum value (e.g., 0.4), ensuring sufficient geometric consistency:

$$\lambda_{\text{shape}} = \max(\lambda_{\text{shape}}, \lambda_{\min}), \quad \lambda_{\text{adv}} = 1 - \lambda_{\text{shape}}. \quad (\text{A.4})$$

The final loss is a weighted combination:

$$\mathcal{L}_{\text{total}} = -\lambda_{\text{adv}} \cdot \bar{\mathcal{L}}_{\text{adv}} + \lambda_{\text{shape}} \cdot \bar{\mathcal{L}}_{\text{shape}}. \quad (\text{A.5})$$

This strategy adaptively reduces adversarial emphasis when the attack saturates (i.e., $\mathcal{L}_{\text{adv}} \downarrow$), and shifts focus to geometry preservation. Empirically, we find this dynamic scheme stabilizes training and improves both realism and attack effectiveness.

A.2. Physical Filtering Module

We introduce a two-stage *Physical Filtering Module* composed of: (1) Topological Pruning (TP), and (2) Structural Denoising (SD), as described in Section 3.4.

Topological Pruning: To eliminate geometrically inconsistent Gaussians while preserving structural continuity, we develop an adaptive density-aware pruning strategy. The local density $\rho(\mathbf{g}_j)$ for each Gaussian \mathbf{g}_j is estimated through its k -nearest neighbors in 3D space. We dynamically determine the removal threshold τ_d as the p -th percentile of density distribution:

$$\tau_d = \text{Quantile}(\{\rho(\mathbf{g}_j)\}_{j=1}^N, p) \quad (\text{A.6})$$

Gaussians satisfying $\rho(\mathbf{g}_j) < \tau_d$ are considered outliers and removed. This percentile-based thresholding automatically adapts to varying object densities without manual parameter tuning.

Structural Denoising: We propose a camera-aware anisotropic filter that jointly optimizes 3DGS scales s_j and opacities α_j . The filtering intensity σ_j for each Gaussian is modulated by its minimum projected distance to camera planes:

$$\sigma_j \propto \min_i \frac{\|R_i x_j + T_i\|_2}{f_i} \quad (\text{A.7})$$

where R_i, T_i, f_i denote the rotation matrix, translation vector, and focal length of the i -th camera. This spatial adaptation ensures stronger smoothing for distant regions while preserving detail in close-range areas. The filtered parameters are obtained through:

$$s'_j = \sqrt{s_j^2 + \sigma_j^2 I}, \quad \alpha'_j = \alpha_j \cdot \frac{\det(s_j)}{\det(s'_j)} \quad (\text{A.8})$$

This dual-phase physical filtering module achieves critical improvements: Noise suppression eliminates floating artifacts, and physical consistency ensures multi-view coherence through camera-aware smoothing.

The final filtered 3DGS representation $\mathcal{G}_{\text{base}}$ maintains geometric fidelity while achieving photorealistic rendering quality, providing a robust foundation for subsequent adversarial optimization.

A.3. Physical Augmentation Module

This section details the exact formulation of the differentiable augmentation components defined in Section 3.5. The

physical augmentation module applies a sequence of four transformations:

$$\mathcal{T} = \mathcal{T}_{occl} \circ \mathcal{T}_{shadow} \circ \mathcal{T}_{photo} \circ \mathcal{T}_{noise}, \quad (\text{A.9})$$

where each sub-transformation models a common source of physical variation. The operations are applied in right-to-left order during optimization.

Imaging Degradation simulates camera sensor noise, which increases with object distance due to atmospheric interference. This degradation is modeled as an additive Gaussian noise function:

$$\mathcal{T}_{noise} = I + \mathcal{N}(0, \sigma^2(d)), \quad (\text{A.10})$$

where I is the original rendered image, $\mathcal{N}(0, \sigma^2)$ represents zero-mean Gaussian noise, and $\sigma(d)$ is the depth-dependent standard deviation:

$$\sigma(d) = \sigma_0 + \gamma \cdot d. \quad (\text{A.11})$$

Here, σ_0 is the base noise level, d represents the pixel-wise depth value, and γ is a scaling factor controlling noise amplification with distance.

Photometric Variation simulates color distortions caused by varying lighting conditions and sensor imperfections. We model this effect using channel-wise affine transformations:

$$\mathcal{T}_{photo} = I_c \cdot \alpha_c + \beta_c, \quad (\text{A.12})$$

where I_c is the original intensity of color channel c , $\alpha_c \sim U(0.9, 1.1)$ represents contrast variation sampled from a uniform distribution, and $\beta_c \sim U(-0.05, 0.05)$ is an additive shift factor.

These transformations ensure that adversarial perturbations remain effective under different lighting conditions.

Shadow Projection used sampling random light source positions and computing penumbra-umbra transitions via sigmoid intensity mapping, we replicated the soft shadow boundaries observed in natural illumination environments.

$$\mathcal{T}_{shadow} = \frac{1}{1 + e^{-\alpha(d(x,y) - d_{th})}}, \quad (\text{A.13})$$

where α controls shadow smoothness, $d(x, y)$ is the depth at pixel (x, y) , and d_{th} is the threshold depth for shadow casting.

Adaptive Occlusion enhances robustness to partial obstructions through random rectangular masks that simulate large-scale object occlusions covering part of the image area.

$$\mathcal{T}_{occl} = \begin{cases} \{0, \text{random}(0, 1)\}, & (x, y) \in \text{occlusion region}, \\ 1, & \text{otherwise.} \end{cases} \quad (\text{A.14})$$

The composite transformation $\mathcal{T} = \mathcal{T}_{occl} \circ \mathcal{T}_{shadow} \circ \mathcal{T}_{photo} \circ \mathcal{T}_{noise}$ establishes a physical augmentation module

during optimization. This phased approach enables the adversarial samples to develop physical robustness, as quantified in Section 4.

A.4. Selective Dimension Optimization

We define three fundamental optimization modes based on parameter space decomposition in the 3D Gaussian Splatting representation:

Geometry-Selected Mode (\mathcal{K}_g): This mode activates all 10 geometry-related dimensions, including position (x, y, z) , scale (s_x, s_y, s_z) , and quaternion rotation (q_w, q_x, q_y, q_z) :

$$\mathcal{K}_g = \{x, y, z, s_x, s_y, s_z, q_w, q_x, q_y, q_z\} \quad (\text{A.15})$$

This mode enables structural manipulation of the object without altering appearance, suitable for settings like geometric camouflage or shape-aware perturbations.

Appearance-Selected Mode (\mathcal{K}_a): This mode only optimizes the 4 appearance-related parameters—color (c_r, c_g, c_b) and opacity (α) :

$$\mathcal{K}_a = \{c_r, c_g, c_b, \alpha\} \quad (\text{A.16})$$

It is ideal for use cases such as 3D-printed objects or painted surfaces, where modifying geometry is impractical or costly.

Full-Dimensional Mode (\mathcal{K}_{full}): For completeness, we denote the full parameter set as:

$$\mathcal{K}_{full} = \mathcal{K}_g \cup \mathcal{K}_a \quad (\text{A.17})$$

which enables unconstrained optimization across the entire 14D space.

Optimization Behavior. As demonstrated in Section 3.6, different modes exhibit different convergence behavior. Geometry-mode reaches high LCR within 30 epochs, while texture-mode requires longer training (up to 200 epochs) but eventually achieves comparable performance. This difference stems from the sensitivity of geometry dimensions (e.g., x, s) to detector outputs, as discussed in our LCR sensitivity analysis (Fig. 6).

Practical Deployment Implications. In scenarios where 3D shape alteration is restricted (e.g., rigid vehicle body), \mathcal{K}_a can be adopted to generate adversarial decals or coatings. For applications involving laser-cut, foam, or parametric shell objects, \mathcal{K}_g can produce printable adversarial shapes while maintaining uniform color.

Further visual examples under different dimension selection strategies are presented in Appendix B.3.

B. Supplementary of Experiments

B.1. Dataset Configuration

Due to the 3DGS generator \mathcal{F}_{3DGS} was pretrained on synthetic scenes. Our framework requires only inference-time



Figure B.1. Selective Dimensions. Mode-selected dimension optimization visualization.

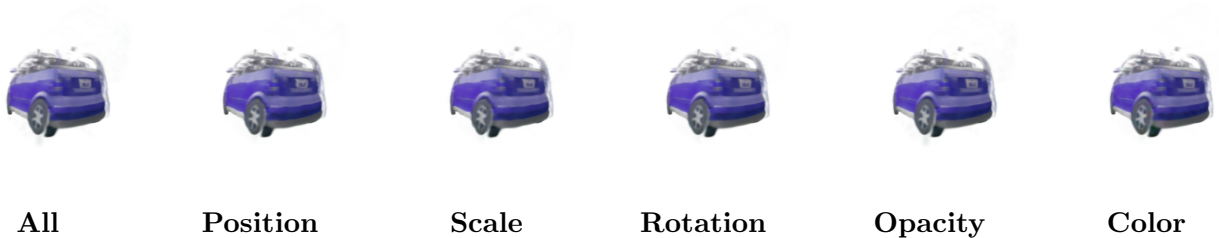


Figure B.2. Selective Dimensions. Single dimension optimization visualization.

multiview inputs. We collect the images from Carla[8], covering: 20 vehicle models with varying geometries, 5 weather conditions (clear, rain, fog, etc.), Multi-scale observations and Full spherical viewpoints (24 azimuth/elevation angles).

B.2. Implementation Details

The 3DGS generation backbone adopts the pretrained LGM architecture [34] with frozen parameters, processing four calibrated views (512×512 resolution) as input. The physical filtering module applies density-based pruning at $\tau_d = 0.105$ percentile threshold, followed by structural Gaussian smoothing, as illustrated by Eq. A.8.

For adversarial optimization, we initialize the learning rate $\eta = 0.03$ with gradient descent over 50 epochs, optimizing all 14 parameters of the 3D Gaussians (positions $x \in \mathbb{R}^3$, rotations $q \in \mathbb{R}^4$, scales $s \in \mathbb{R}^3$, colors $c \in \mathbb{R}^3$, opacity $\alpha \in \mathbb{R}^1$) under the combined loss from Eq. 5. The physical augmentation module probabilistically applies transformations with $\gamma = 0.005$ for scaling factor and $p_{size} = 0.1$ for occlusion size.

All experiments are conducted on an NVIDIA RTX 4090 GPU with PyTorch 2.1 + CUDA 11.8, where each adversarial optimization completes within 1 minute.

B.3. Selective Dimension Optimization

Our experiments investigate the sensitivity of different dimensions in 3DGS under adversarial optimization. The part-based optimization comparison (Fig. 6a) reveals that

modifying geometric dimensions achieves a high LCR within a few training iterations. This indicates that 3DGS is particularly sensitive to geometric perturbations, making it highly susceptible to adversarial attacks in this domain. In contrast, texture-based optimization requires more training steps to reach an optimal adversarial effect but ultimately surpasses geometric perturbations in overall LCR. This suggests that while geometry is more straightforward to manipulate for quick adversarial impacts, texture perturbations offer more effective long-term deception, as shown in Fig. B.1.

Further analysis in all-dimension optimization (Fig. 6b) demonstrates that different dimensions exhibit varying degrees of adversarial sensitivity. The position x and scale s dimensions show high sensitivity, meaning even minor perturbations in these attributes significantly impact the rendered adversarial object. Conversely, opacity α and RGB c color dimensions exhibit lower sensitivity, requiring more extensive modifications to influence the detection model. Notably, the quaternion rotation q dimension is the least sensitive, requiring the most training iterations yet achieving the lowest LCR in 400 epochs. The visualized results are shown in Fig. B.2. This implies that 3DGS representations are more resistant to adversarial attacks targeting 3DGS rotational attributes, likely due to their global influence on object orientation rather than direct appearance modifications.

These findings highlight the importance of selecting optimal adversarial dimensions for attack optimization. While

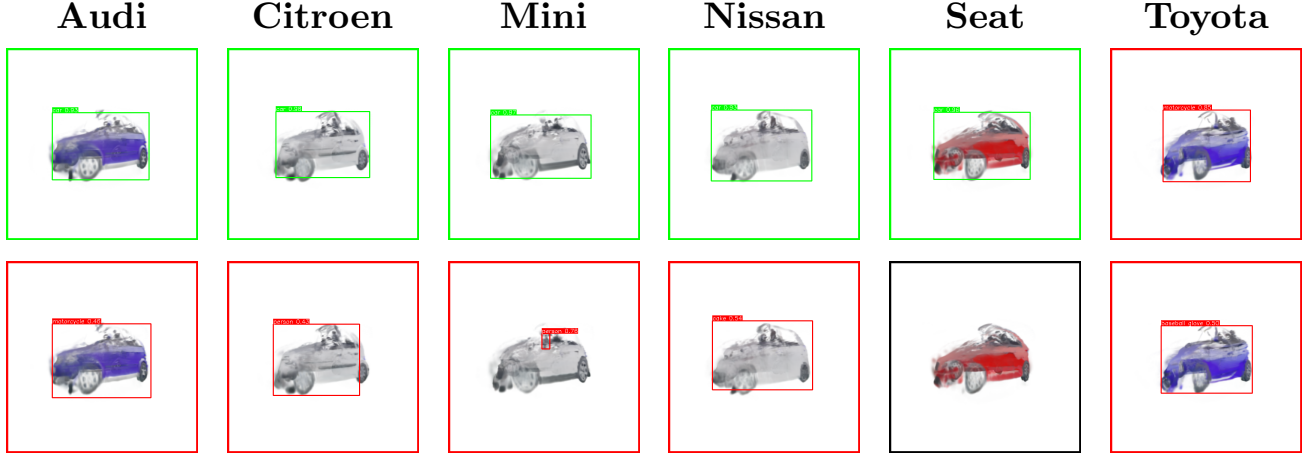


Figure B.3. Adversarial Effectiveness of 3DGAA Across Different Vehicle Types.

geometric perturbations offer immediate adversarial benefits, optimizing texture features leads to superior attack efficacy. Moreover, identifying sensitive dimensions x, s can help refine attack strategies, ensuring effective adversarial perturbations while minimizing unnecessary computational overhead.

B.4. Object Generalization

A critical aspect of adversarial attacks is their ability to generalize across different object categories. To evaluate the generalization capability of 3DGAA, we apply our adversarial optimization framework to multiple vehicle types, including sedans, SUVs, trucks, and buses. As shown in Fig. B.3, the results demonstrate that 3DGAA consistently reduces the detection confidence of different vehicle types, confirming its robustness and transferability across diverse 3D object geometries.

These findings indicate that the adversarial perturbations learned by 3DGAA effectively adapt to various object structures, ensuring broad applicability in real-world scenarios. Moreover, the ability to generalize across object categories strengthens the practicality of 3DGAA in autonomous driving security research, where adversarial robustness must be considered for a wide range of vehicle shapes and sizes.

B.5. Multi-Angle Visualization of 3DGAA Results

Figures B.4 and B.5 provide extended multi-perspective visualizations of our method’s capability to maintain structural authenticity while achieving adversarial effectiveness. Figure B.4 demonstrates the original 3DGS reconstructions across 12 representative viewpoints, highlighting the baseline geometric accuracy and texture fidelity. Correspondingly, Figure B.5 showcases the adversarial counterparts under identical viewing conditions, where optimized texture patterns consistently mislead detectors without introducing noticeable visual disparity.

Table B.1. Realism scores of different adversarial and vanilla textures from participants.

Methods	Scores	Methods	Scores
Vanilla	9.6	Random	1.1
CAMOU	2.9	UPC	6.4
DAS	3.9	FCA	2.3
DTA	3.2	ACTIVE	6.0
3DGAA*	7.1	3DGAA	7.9

3DGAA*: Appearance-Selected mode.

The side-by-side comparison reveals two key observations: (1) The adversarial textures preserve high-frequency surface details comparable to original patterns, ensuring physical plausibility, (2) Adversarial effectiveness remains stable across extreme viewing angles, confirming the 3DGAA optimization’s robustness to perspective variations. These visual results complement our quantitative analyses by demonstrating the spatial consistency of geometric reconstruction and adversarial pattern generation.

B.6. Human Perception

To further evaluate the realism of adversarial textures generated by 3DGAA, we conducted a human perception study with 50 volunteers. Each participant was shown a series of adversarially perturbed vehicle images and was asked to rate the perceived realism on a 1 to 10 scale, where 10 indicates that the texture appears completely natural, resembling standard vehicle paint or patterns. 1 indicates that the texture is highly unnatural and adversarially modified. Each volunteer was presented with a randomized set of images, including both adversarially perturbed and vanilla textures. This study aimed to assess whether adversarial textures can remain imperceptible to human observers, as a key compo-

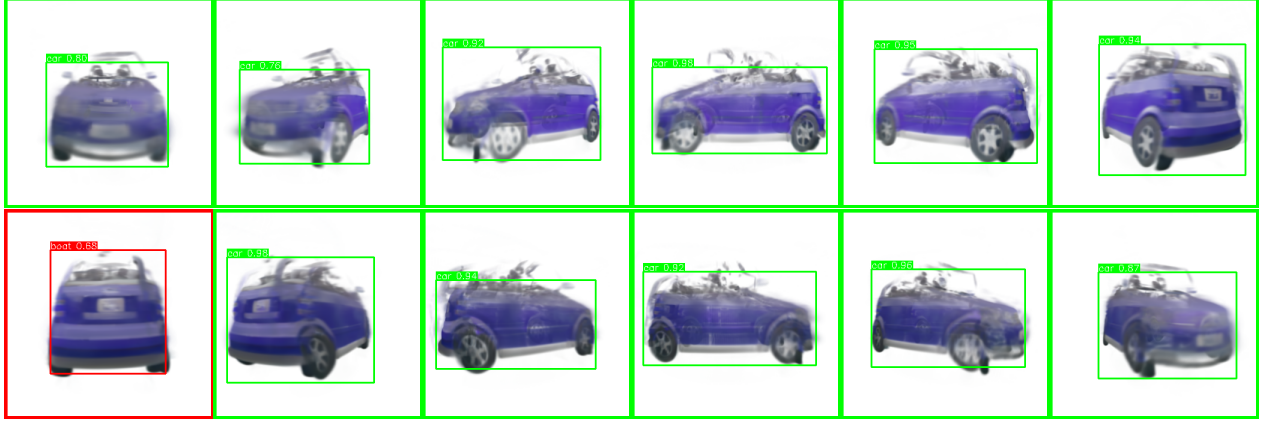


Figure B.4. Multi-View Visualization of Original 3DGS Reconstructions: Twelve representative viewpoints demonstrating baseline geometric accuracy and texture fidelity.

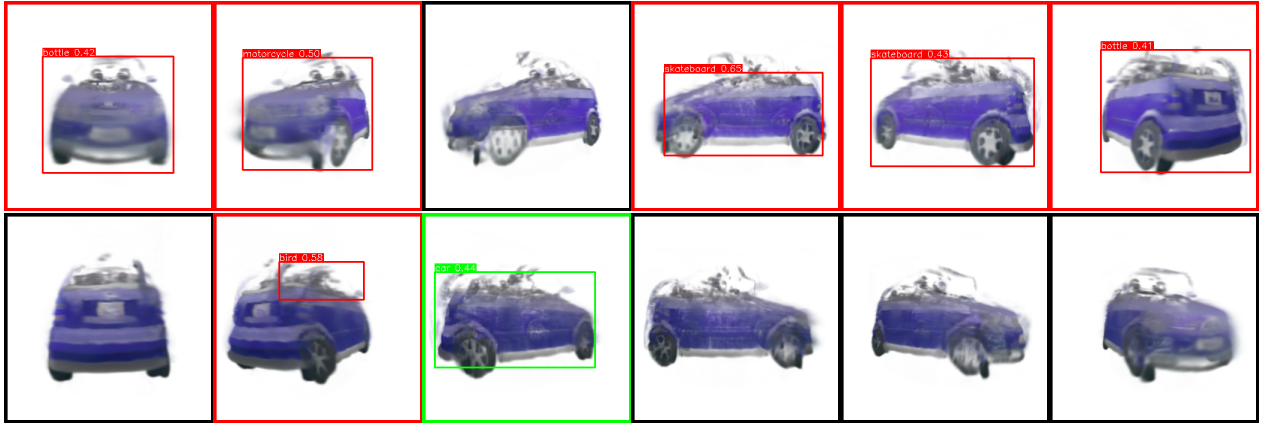


Figure B.5. Consistent Adversarial Effects Across Viewing Angles: Corresponding adversarial 3DGS visualizations under identical viewpoints, showing maintained structural integrity while evading detection.

ment of maintaining physical realism in real-world adversarial attacks.

We analyze the collected ratings by computing the average realism score per condition and compare different adversarial and vanilla textures. The results presented in Table B.1 demonstrate the superior realism of our proposed 3DGAA method compared to existing adversarial attack approaches. Notably, 3DGAA achieves a significantly higher realism score of 7.9, outperforming prior methods such as ACTIVE (6.0), UPC (6.4), and DTA (3.2), indicating that adversarial perturbations generated by 3DGAA are less perceptible to human observers. The appearance-selected variant, 3DGAA* (7.1), further validates the effectiveness of our approach, demonstrating that the texture modifications in 3DGAA contribute to improved realism while maintaining adversarial effectiveness. Compared to real vehicle textures (Vanilla: 9.6), our method achieves the closest resemblance, confirming that our *Physical Filtering Module* and *Physical Augmentation Module* successfully reduce un-

realistic artifacts. Furthermore, conventional adversarial texture-based methods, such as CAMOU (2.9), DAS (3.9), and FCA (2.3), exhibit significantly lower realism scores, primarily due to their reliance on large-scale texture distortions that lack physical consistency. The extreme case of Random (1.1) highlights that naive perturbations are easily identifiable as artificial, further reinforcing the necessity of structured optimization in adversarial texture generation. These results demonstrate that 3DGAA achieves a superior balance between adversarial robustness and realism, making it more applicable to real-world scenarios where physical reality is crucial.

C. Discussion

C.1. Adversarial Effectiveness is Derived from 3DGAA

The adversarial effectiveness of 3DGAA originates from its explicit adversarial optimization, which differentiates it

from conventional 3D Gaussian Splatting (3DGS) representations. While 3DGS naturally introduces slight distortions in shape and texture due to the limitations of generation and sampling, these variations do not inherently contribute to adversarial behavior. The core objective of 3DGS is to reconstruct high-fidelity 3D objects from multi-view images, ensuring that the generated representation maintains visual consistency rather than misleading object detection models.

In contrast, 3DGAA explicitly optimizes the adversarial properties of the object by introducing targeted perturbations in texture and geometry. This process is guided by an adversarial loss function, which systematically reduces detection confidence while preserving the object’s structural integrity. To achieve this balance, a shape preservation constraint is integrated into the optimization process, preventing excessive geometric distortions that could otherwise compromise the physical reality of the adversarial object. As a result, 3DGAA generates objects that exhibit strong adversarial effectiveness maintain realistic physical attributes, making them highly transferable across different detection models and environmental conditions.

C.2. Generalization to Non-Vehicle Objects

The framework of 3DGAA is inherently designed to be object-agnostic, allowing its application beyond vehicle-related adversarial scenarios. While our experimental evaluations primarily focus on vehicles, the underlying optimization process operates on fundamental 3D attributes, including position, scale, rotation, opacity, and color. These attributes are not limited to any specific category of objects, suggesting that the method can be generalized to a wide range of targets.

The physical filtering and augmentation modules incorporated in 3DGAA are formulated independently of object semantics. These modules refine the adversarial object while ensuring adaptability to varying physical and environmental conditions, reinforcing the method’s applicability to non-vehicle objects such as pedestrians, animals, or urban infrastructure. Extending 3DGAA to diverse object categories opens promising directions for future research, particularly in adversarial robustness across different real-world scenarios.

C.3. Optimization Efficiency

The efficiency of 3DGAA is a result of its computational design and strategic optimization approach. Unlike conventional adversarial attack frameworks that rely on texture-based deformations, 3DGAA operates on 3DGS representations, significantly reducing computational overhead. By leveraging the Gaussian-based parameterization, the attack directly optimizes object attributes without needing explicit surface reconstruction, leading to faster convergence and lower memory consumption. Usually, we complete an en-

tire generative-adversarial process in less than one minute.

Additionally, the optimization process in 3DGAA follows a structured loss-balancing strategy. The adversarial loss and shape preservation loss are dynamically weighted, ensuring that the optimization process remains stable while effectively guiding the object toward an adversarial state. This selective gradient update mechanism minimizes unnecessary modifications, accelerating convergence without sacrificing attack strength.

Furthermore, the physical augmentation module is designed to enhance optimization stability by progressively introducing perturbations. This staged approach prevents destabilization during training, contributing to the overall computational efficiency of 3DGAA. Combining these design choices ensures that 3DGAA achieves high attack performance while maintaining physical reality in real-world adversarial scenarios.

C.4. Ethical Considerations

Potential Societal Risks. Our work introduces **3DGAA**, a 3D Gaussian-based framework for generating physically realistic adversarial objects. While this research aims to advance understanding of model vulnerabilities and robustness in safety-critical applications such as autonomous driving, it inherently poses potential risks if misused. These include: (1) intentional deployment of adversarial objects in real-world environments to cause sensor-level misperception, (2) disruption of autonomous navigation systems through physically disguised threats, and (3) security concerns arising from the transferability of attacks across models and viewpoints.

Mitigation and Safeguards. To mitigate misuse, we emphasize the following safeguards: (1) our attacks are conducted strictly in controlled simulation environments or on miniature-scale physical setups, without field deployment; (2) we do not release attack code or physical models publicly at this stage; and (3) our method is also intended to guide future development of more robust perception systems and defense techniques. Moreover, we incorporate physical realism constraints and shape fidelity to reduce the feasibility of applying large-scale, arbitrary perturbations.

Responsible Disclosure and Reproducibility. We advocate for responsible disclosure and reproducibility: the proposed attack can serve as a benchmark tool for stress-testing detection systems under worst-case conditions, and the 3D Gaussian representation supports explainable diagnostics. We believe that transparency around such vulnerabilities can foster long-term security through proactive system hardening, not exploitation.

Use of Human-derived Data. Our work includes a perceptual user study (Appendix B.6) in which human raters evaluate the realism of rendered 3D objects under different con-

ditions. This evaluation was conducted anonymously and non-invasively, without collecting any personally identifiable information, demographic attributes, or biometric data. Participants were not exposed to offensive or sensitive content, and their involvement was limited to providing visual realism ratings on a 10-point scale. Given the benign and low-risk nature of this evaluation, formal IRB approval was not sought, in line with common practice for perception-focused visual studies in computer vision.